Whistler Waves Driven by Anisotropic Strahl Velocity Distributions: Cluster Observations

A. F- Viñas*, C.Gurgiolo†, T. Nieves-Chinchilla*, S. P. Gary** and M. L. Goldstein*

*Geospace Physics Laboratory, Code 673, NASA Goddard Space Flight Center, Greenbelt, MD
†Bitterroot Basic Research, Hamilton, MT
**Los Alamos National Laboratory, Los Alamos, NM

Abstract. Observed properties of the *strahl* using high resolution 3D electron velocity distribution data obtained from the Cluster/PEACE experiment are used to investigate its linear stability. An automated method to isolate the *strahl* is used to allow its moments to be computed independent of the solar wind *core+halo*. Results show that the *strahl* can have a high temperature anisotropy ($T_\perp/T_\parallel \gtrsim 2$). This anisotropy is shown to be an important free energy source for the excitation of high frequency whistler waves. The analysis suggests that the resultant whistler waves are strong enough to regulate the electron velocity distributions in the solar wind through pitch-angle scattering.

Keywords: solar wind, strahl, whistler waves
PACS: 52.35.-g

1. INTRODUCTION

The typical collisional mean free path for solar wind electrons at 1 AU is of the order of 10^8 km which is comparable to the system length scale. This suggests that these electrons are not in thermal equilibrium and should contain a significant non-thermal component, as is indeed seen in the shape of its velocity distribution function (VDF). The electron VDF is regulated by the conditions in the solar corona from which the electrons emanate, by the nature of the scattering processes between the source and the measurements location (e.g.,Coulomb collisions, wave-particle interactions), and by the dynamical forces due to the global and local magnetic and electric fields. Detailed observations of the electron VDFs can then provide information about the propagation conditions in the interplanetary medium and to some extent can serve as a probe for conditions in the solar corona itself.

The solar wind is generally comprised of three main components: the *core*, a thermally isotropic population observed below 10-15 eV and containing about 95% of the overall density; the *halo*, a non-isotropic suprathermal population observed between 12 eV and 100 eV, and the *strahl*, a highly field-aligned beam-like population seen above 50 eV and often exhibiting a temperature anisotropy ($T_\perp/T_{||}$) of 2 or more. Together the *halo* and *strahl* comprise the main source of the heat flux transport in the solar wind. A fourth population is sometimes observed when the measurement point is magnetically connected to the bow shock. This is either electrons which have reflected off the shock or the leakage of post-shocked electrons back into the upstream region.

Previous observational and theoretical studies have provided important clues about the processes that regulate the *strahl* in the solar wind. Lemons and Feldman [1] have investigated how collisions modify exospheric models of solar wind suprathermal electron pitch-angle distributions (PADs) and have compared their results with measurements at 1 AU. Their results show PAD widths which are larger than those predicted by exospheric models, but are still not large enough to account for the PADs measured in typical fast- and slow- solar wind streams. They suggested that another source of scattering such as wave-particle interactions must play a role in the broadening of the solar wind pitch-angle distribution. The width of the PAD is therefore a measurable property that provides insights into the processes responsible for the angular broadening of the *strahl* VDFs [2, 3, 4, 5, 6]. Observations of the *strahl* in high-speed solar wind at intermediate and high latitudes and at larger radial distances on Ulysses found its angular width to be broader than that observed in the ecliptic plane [5]. Recent theoretical work on wave-particle resonant interactions with electrons in the solar wind has shown that whistler waves are capable of generating suprathermal electrons sufficiently broad in pitch-angle to be consistent with the observations of non-thermal VDFs at 1 AU [7, 8]. The kinetic model used (i.e., quasi-linear theory via pitch-angle diffusion) in these formulations includes not only wave-particle resonant interactions, but also Coulomb collisions and the mirror force experienced by the electrons as they propagate into a decreasing magnetic field.

The intensity level of enhanced whistler waves determines the characteristics of their power spectrum and the nature of their spectral properties determines which

CP1216, *Twelfth International Solar Wind Conference,*
edited by M. Maksimovic, K. Issautier, N. Meyer-Vernet, M. Moncuquet, and F. Pantellini
2010 American Institute of Physics 978-0-7354-0759-6/10/$30.00

electrons can undergo wave-particle interactions. There are at least four sources of whistler wave excitation: the whistler heat-flux instabilities driven by the relative drifts among the electron components, the anisotropic whistler instabilities which are driven by the temperature anisotropy ($T_\perp > T_\parallel$or $T_\perp < T_\parallel$) of the electron components, and the classical scenario of MHD turbulent cascade or wave-wave interactions. In this last scenario, fluctuations in the plasma are driven at some large "outer" scale and then decay by exchanging energy with fluctuations at nearby spatial scales resulting in a net flow of energy to smaller spatial scales (larger k). This cascade of energy occurs over an inertial subrange of k-space and it has been shown to follow a Kolomogorov scaling of $\mathrm{k}^{-5/3}$. At even smaller scales the spectrum becomes steeper due to interaction with the plasma ions and/or electrons via either cyclotron, Landau, or transit time damping on the species. These are the scales at which the wave-particle interaction plays a role in regulating and shaping the particle VDFs since they represent the ultimate fate of the cascade of energy.

The overall anisotropy and heat-flux transport of the total solar wind VDF can be attributed to the presence of the *halo* and *strahl*. In the presence of the *strahl* the solar wind VDF becomes anisotropic with $T_\parallel > T_\perp$[4, 9, 10]. Using Wind data at 1AU in the ecliptic plane [11] has pointed out that the overall temperature anisotropy ($T_\perp/T_\parallel$) depends mainly on Coulomb collisions (strong correlation between the temperature anisotropy and the collisional age) and therefore plays a part in the regulation of the solar wind VDF. Consequently they also find that the electron heat-flux shows an upper bound that is inversely proportional to the collisional age. It is important to point out that the [11] results are strictly defined for the total solar wind VDFs and do not distinguish between the various electron components (*core*, *halo*, *strahl*, reflected/leakage).

Linear and particle-in-cell simulation studies on the whistler instabilities have been carried out by many authors (e.g., [12, 13, 14, 15, 16], and references within among others). An overall summary of these investigations clearly shows that the temperature anisotropy $T_\perp/T_\parallel > 1$ provides the most sensitive free energy source for the generation and excitation of whistler waves. However, these studies have assumed that the anisotropy exists in the *core* electron VDF. This is certainly arguable since the *core* electrons are Coulomb collision dominated (e.g., [3, 1]) and therefore are isotropic in their own frame. It is true that previous results suggesting anisotropic *core* distributions have been reported in the scientific literature (e.g. [9]), but these anisotropies are first in the opposite sense ($T_\perp < T_\parallel$) consistent with most general observations of the overall electrons in the solar wind, and second are seen in the energy range below 150 eV which is hardly representative of the *core* electrons which are usually below 15 eV. If anything, these anisotropies reflect that of the overall solar wind VDF or at most that of the *core+halo*.

In this paper we will use a linear plasma wave analysis of the *strahl* to illustrate what effect a highly anisotopic *strahl* with $T_\perp > T_\parallel$ has on the stability of the total solar wind electron VDFs. Our analysis will be fully constrained by the observed measurements without invoking any arbitrary or free parameters. The implications of this result will be discussed.

2. CLUSTER DATA

The stability analysis presented in this paper is based on a set of data taken on Jan 10, 2004 between 06 to 07 UT. During this time period the Cluster spacecraft were in the solar wind with no apparent local connection to the bow shock (no presence of reflected/leakage particles).

The electron data were obtained from the Cluster-2 PEACE Low Energy Electron Analyzer (LEEA) [17]. At the time the PEACE analyzer was returning full three-dimensional electron VDFs every 4 seconds (satellite spin period) with a resolution of $30\mathrm{E}\times12\theta\times32\phi$ bins The energy range covered was from 7.3 to 3952 eV in equal logarithmically spaced steps and the angular coverage was a full 4π steradians. Moment calculations used in the paper were computed according to the standard method described in Viñas and Gurgiolo [18]. This takes into account corrections for the spacecraft potential using the spin averaged potential supplied by the Electric Field and Wave (EFW) Experiment [19] plus a 1.5 V contact potential. The total potential, which varies with the local plasma conditions, was on the order of 5 V (6.5V when the contact potential is included). High resolution magnetic field data (67 samples/s) from the FGM experiment [20] were obtained from the Cluster Active Archive (CAA) and used in for local wave analysis. Conversion of the moments to a magnetic field coordinate system used spin averaged values of the field. The proton data used in the dispersion analysis was obtained from the CIS experiment (prime parameters) [21] onboard Cluster-1, the CIS sensor on Cluster-2 having failed. The use of Cluster-2 for the electron data was made because the instrument was returning data at higher angular resolution on that spacecraft than on Cluster-1. Close similarities between the PEACE moments computed from both Cluster-1 and -2 suggests that using CIS data from Cluster-1 should present no problem in the analysis.

3. STRAHL ANALYSIS

The isolation of the *strahl* from the other solar wind components is accomplished by an automated 3D graphical-

numerical method which works in both the energy and angular domains and on an event by event basis. The VDF in spherical coordinates is represented by a function $f(v,\theta,\phi)$, where the independent variables are the velocity, polar angle, and azimuthal angle respectively. In this

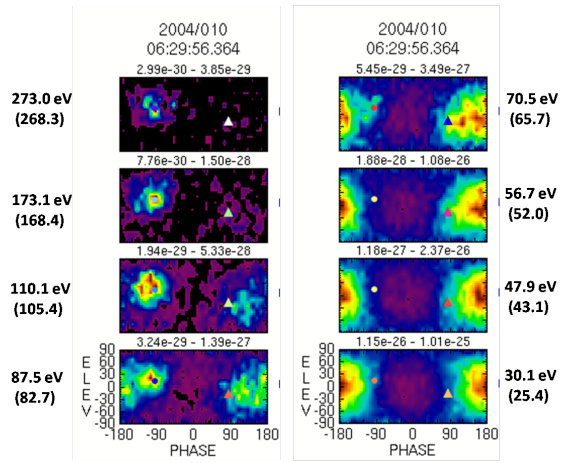

FIGURE 1. Set of 8 skymaps showing the angular mapping for a subset of the 30 energy steps in a VDF. The energy steps shown are not contiguous

space the VDF can be displayed by a set of skymaps, plots of the angular variation of the VDF at a fixed velocity (energy). An example set of skymaps is shown in Figure 1. Each panel contains data from a fixed energy shell of the VDF. Azimuth is plotted along the x-axis and elevation is plotted along the y-axis. The Sun is located in the plane defined by $\phi = 0$. The energy corresponding to each plot is shown to the right- and left- sides of the figure. The potential corrected energy is shown in parentheses. Annotation at the top of each plot shows the maximum and minimum values of the VDF in the plot. The color scale for each plot runs linearly from the minimum to the maximum value, thus you cannot directly compare the intensities between plots simply by color. The circle (•) and triangle (▲) symbols in each plot are the projection of the head and tail respectively of the spin averaged magnetic field vector. The population of particles centered on $\pm 180^\circ$ at the lowest four energies in Figure 1 are part of the solar wind *core+halo*. (Since we are not distinguishing between the two we will always refer to them together.) At 87.5 eV the distribution visually shifts and becomes field aligned. These are the *strahl* electrons which begin to significantly dominate the *core+halo* population at and above this energy. The *strahl* extends up through 273 eV in the skymaps.

To isolate the *strahl* we first select the VDF at the energy channel where there is a clear field-aligned signature moving anti-sunward. We then mask an angular region about the magnetic field projection on which the *strahl* is centered and zero out all data outside the mask. The angular width of the mask is made large enough to contain the full *strahl* signature in the skymap. This procedure is carried out on all energies above the initial energy. In general the energy at which the *strahl* dominates remains fixed within the time period being analyzed. Moments can then be produced for the isolated distribution [18]. We recognize that there will be some *core+halo* electrons mixed with the *strahl* but their contribution must be negligible for the distibution to be seen shifted in velocity space. The isolation technique can be used to isolate other populations present in the data as well.

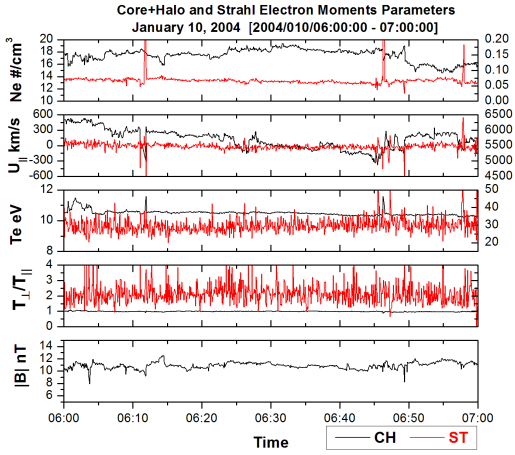

FIGURE 2. Electron density, parallel velocity, total temperature, and temperature anisotropy for both the *core+halo* and *strahl* over the Jan. 10, 2004 event. Bottom panel show the total magnetic field.

Figure 2 shows plasma moments for both the *strahl* and *core+halo* populations for the January 10, 2004 event. The *core+halo* populations were isolated in the same manner as used for the *strahl* except the circle center is located at $(\phi,\theta) = (180^\circ, 0^\circ)$. In the plasma parameter plots red traces are used for the *strahl* and black for the *core+halo*. With the exception of the temperature anisotropy, the *strahl* parameters are plotted against the right-hand y-axis.

During the time period shown the spacecraft appears to be not magnetically connected to the bow shock as evidenced by the lack of reflected/leakage electrons and no obvious ULF frequency waves in the magnetic field. Noticable in the figure is the temperature anisotropy of the *strahl*, which averages about 2. The *core+halo* is as expected isotropic with a temperature anisotropy close to 1. Although it is probably obvious, it should be emphasized that the temperature depends on the electron population or populations included in the moment computation. The temperature is the spread in velocity about the average bulk velocity and both are dependent on the included

populations. This is why the temperature anisotropy in the total solar wind distribution (i.e., *core+halo+strahl*) has $T_{||} > T_{\perp}$ while the *strahl* itself can show a temperature anisotropy of $T_{\perp} > T_{||}$. This is illustrated in Figure 3 which shows plots of the full solar wind (top panel) and isolated *strahl* (bottom panel). Both plots are shown in the frame of reference of the solar wind. In the upper plot central portion of the VDF, which is visually isotropic, is the *core+halo.* The elongation of the distribution to the right is due to the *strahl* leading to a $T_{||} > T_{\perp}$.We estimate an angular width of the strahl to be about $\pm 60^{\circ}$ on the average in this frame. The *strahl* when plotted in its own reference frame is actually broader and elongated in the perpendicular direction which is indicative of a temperature anisotropy greater than 1 as is seen in Figure 2.

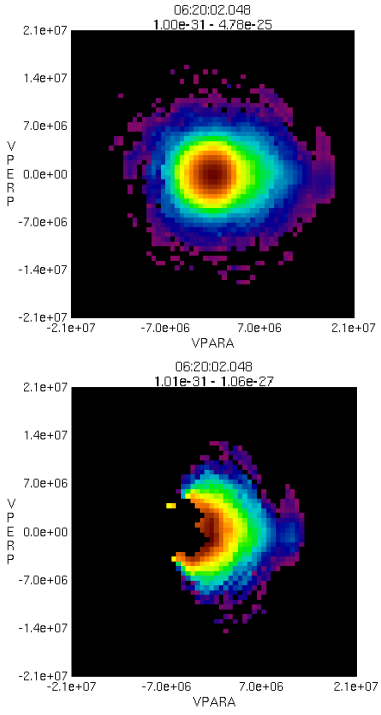

FIGURE 3. Plots of the full solar wind VDF (top) and of the *strahl* (bottom) from one spin of data during the Jan 10. period.

4. DISPERSION ANALYSIS

To investigate the role that the temperature anisotropy of the *strahl* plays in the stability of the overall solar wind electron VDF, the basic *in-situ* moments (density, velocity, temperature) of the the *core+halo* and *strahl* must be computed individually. To do this requires the ability to isolate the two populations which was described in the last section. The electron and magnetic field data shown in Figure 2together with the CIS proton data were used to derive the parameters required in the dispersion analysis. These are shown in Figure 4. Plotted are: the ratio of plasma to cyclotron frequency, the *core+halo* and *strahl* density normalized to total density, the parallel drift velocity of the *strahl* normalized to the *core+halo* parallel thermal velocity, the parallel $\overline{\beta}_{||e}$ for the *core+halo* and *strahl* and the parallel $\overline{\beta}_{||p}$ of protons. The parallel plasma $\overline{\beta}_{||s}$ is representative of the parallel temperature and is defined as $\overline{\beta}_{||s} = \left(8\pi n_{etot}\, T_{||s}/B^2\right)$ for each plasma component.

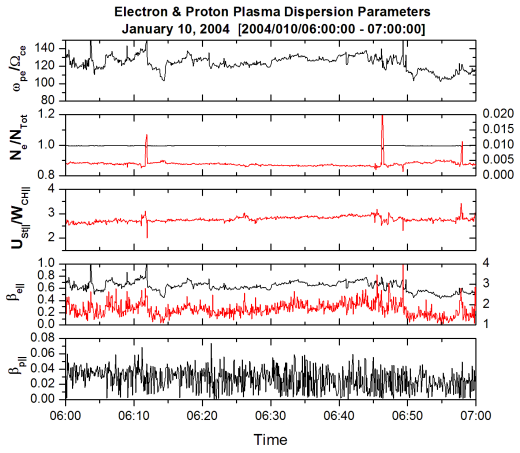

FIGURE 4. Plots of the plasma parameters used in the linear stability analysis. Black traces refer to parameters associated with the *core+halo* and red traces those associated with the *strahl*.

The dispersion analysis assumes a plasma composed of an isotropic *core+halo* a field-aligned, anisotropic *strahl* and a proton population in a homogeneous medium with a constant magnetic field. The calculation was carried out by numerically solving the dispersion relation [22] for parallel propagating electromagnetic whistler waves given by:

$$D(k,\omega) = 1 - \frac{k^2c^2}{\omega^2} + \frac{k^2c^2}{\omega^2}\sum_s S_s^{\pm}(k,\omega) = 0 \qquad (1)$$

where the summation over the subscript s represents the particle species, ω is the complex frequency (i.e., $\omega = \omega_r + i\gamma$), k is the parallel wave vector, and c is the speed of light. $S_s^{\pm}(k,\omega)$ is a function defined as

$$S_s^{\pm}(k,\omega) = \frac{\omega_{ps}^2}{k^2c^2}\left[\xi_s Z\left(\xi_s^{\pm}\right) + \left(1 - \frac{T_{||s}}{T_{\perp s}}\right)\frac{Z'\left(\xi_s^{\pm}\right)}{2}\right]$$

where $Z\left(\xi_s^{\pm}\right)$ is the Fried and Conte plasma dispersion function and $\xi_s^{\pm} = \left(\omega - ku_{||s} \pm \Omega_{cs}\right)/\left(kv_{||s}\right)$ is a parameter that represents the resonance condition. The param-

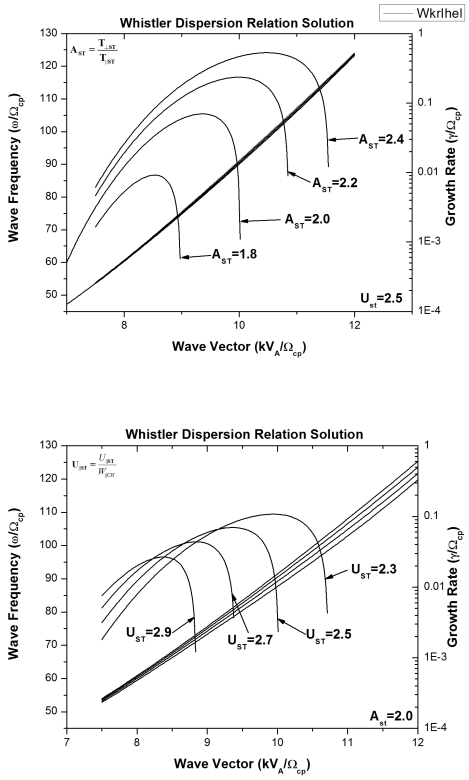

FIGURE 5. Dispersion curves computed from 1. Plots shows the frequency and growth rates for whistler waves normalized to the proton cyclotron frequency Ω_{cp} in units of the proton inertial lengths V_A/Ω_{cp}. Upper plot shows the growth rates as a function of *strahl* temperature anisotropy while the lower plot shows the growth rates as a function of the *strahl* normalized parallel drift velocity.

eters $u_{\|s}$ and $v_{\|s}$ are the parallel drift and thermal velocities respectively for particles of species s. The numerical calculations are carried out in the frame of the protons. Both quasi-neutrality and zero-current have been imposed. The resonance condition for electrons in 1 occurs choosing the "+" sign which denotes right-hand polarization. The resonance condition with electrons then becomes $ku_{\|e} = \omega_r - |\Omega_{ce}|$. Notice that this condition shows that in order for electrons to resonate with parallel propagating whistler waves ($|\Omega_{cp}| < \omega_r < |\Omega_{ce}|$), they must be propagating anti-parallel to the waves.

Figure 5 shows the real frequency and growth rates for whistler waves derived from 1. It is clear that whistler waves (with frequencies in the range of $60 \leq \omega_r/\Omega_{cp} \leq 120$) are excited by a *strahl* temperature anisotropy of 2. The peak in the growth rate decreases and the overall range narrows as the anisotropy decreases. The reverse occurs as the temperature anisotropy increases. The effect of the parallel drift velocity is opposite to that of the temperature anisotropy; the peak in the growth rate decreases and the overall range narrows as the drift velocity increases with the opposite occurring when the drift decreases. This is due to the fact that the temperature anisotropy is kept fixed at a value of 2, and as the drift velocity decreases the effective number of particles that come into resonance with the waves increases. Of the two free energy sources, the whistler wave excitation is more sensitive to the *strahl* temperature anisotropy.

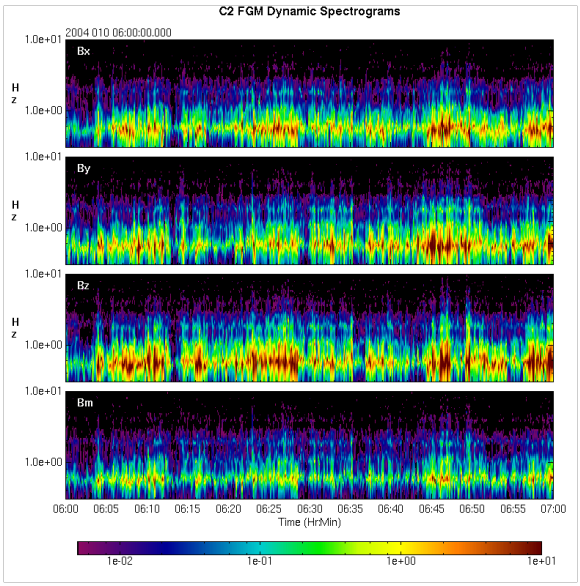

FIGURE 6. Plots of the magnetic power spectra for all components and total field. This shows peaks in the spectra consistent with whistler waves through most of the time period being looked at.

We have also looked at the possibility of driving the whistler instability using the total VDF since it has $T_\perp/T_\| \simeq 0.6-0.8$ and driving the whistler *heat-flux* instability by the relative drifts between the core+halo and an isotropic strahl. The analysis showed that under the conditions seen in the data neither instability is viable. At a minimum they required a parallel electron $\overline{\beta}_{\|e}$ greater than 4 while the measured values are in the 1.5-2 range.

It is interesting to look at the magnetic field data to see if there are any features which might indicate the presence of whistler waves during the time period analyzed. Figure 6 shows a set of dynamic power spectra of the magnetic field components and total field at Cluster-2 over the analysis time period derived from the high resolution FGM data. Each spectra was formed from 512 points (~7.5s) with the spectra window advancing 128 points (~1.9s) at each step. Spectra were computed using a Maximum Entropy algorithm. The plots show a consistent peak in the range 0.5-0.6 Hz across most of the time period. While we cannot at this time definitely say that these are whistler waves, they are at least consistent with what would be expected for whistler waves.

5. DISCUSSION AND SUMMARY

What we have presented above is a set of local observations on the stability of the *strahl* without merging this into a larger overall picture of the dynamics of propagation of the solar wind as it propagates outward from the Sun. This is well beyond the scope of this paper and involves questions such as what sustains the *strahl* temperature anisotropy and what effects do the whistler waves generated by the *strahl* play in the overall dynamics of the solar wind electrons.

The data suggests that the *strahl*, at least during the time frame looked at is approximately in a state of "equilibrium". The energy being dissipated by the *strahl* in driving the whistler waves is being somehow compensated for to sustain the temperature anisotropy. One possible scenario is the following. The *strahl*, initially isotropic, propagates away from the Sun. It encounters waves generated in the turbulent cascade of low frequency MHD Alfvènic waves. This wave field contains both inward and outward propagating fluctuations which cascade down into the whistler regime and electron scales [23]. The inward propagating waves are able to resonate with the *strahl* causing a pitch-angle scattering, creating the observed temperature anisotropy. The anisotropic *strahl* then becomes itself unstable driving whistler waves. The system enters an "equilibrium" state when the energy supplied by the cascade balances that lost through the instability.

Significant and more precise work must be done to fully consider all of the ramifications. This will probably require the use of particle-in-cell simulations and/or self-consistent kinetic transport models that includes wave-particle interactions.

ACKNOWLEDGMENTS

We would like to thank the PEACE, FGM, CIS and EFW teams for use of their data. We also acknowledge the Cluster Active Archive as a source of some of the data used. AFV and MLG would like to acknowledge the support of NASA headquarters to the Cluster mission and the PEACE experiment. TNC would like to thank ORAU for her support through the NASA Post-doctoral program. AFV would like to thank John Dorelli for his comments and pleasant discussions.

REFERENCES

1. D. Lemons, and W. Feldman, *J. Geophys. Res.* **88**, 6881 (1983).
2. W. C. Feldman, J. R. Asbridge, S. J. Bame, M. D. Montgomery, and S. P. Gary, *J. Geophys. Res.* **80**, 4181 (1975).
3. W. C. Feldman, J. R. Asbridge, S. J. Bame, J. T. Gosling, and D. Lemons, *J. Geophys. Res.* **83**, 5285 (1978).
4. W. G. Pilipp, and et. al., *J. Geophys. Res.* **92**, 1075 (1987).
5. C. M. Hammond, W. C. Feldman, D. J. McComas, and R. J. Forsyth, *Astron. Astrophys.* **316**, 350 (1996).
6. K. Ogilvie, R. Fitzenreiter, and M.Desch, *J. Geophys. Res.* **105**, 27277 (2000).
7. C. Vocks, and G. Mann, *Astrophys. J.* **593**, 1134 (2003).
8. C. Vocks, R. P. Lin, and G. Mann, *Astrophys. J.* **627**, 540 (2005).
9. W. G. Pilipp, and et. al., *J. Geophys. Res.* **92**, 1093 (1987).
10. W. G. Pilipp, and et. al., *J. Geophys. Res.* **92**, 1103 (1987).
11. C. Salem, D. Hubert, C.Lacombe, S. D. Bale, A. Mangeney, D. E. Larson, and R. P. Lin, *Astrophys. J.* **585**, 1147 (2003).
12. S. P. Gary, E. Scieme, J. Phillips, and W. Feldman, *J. Geophys. Res.* **99**, 23391 (1994).
13. S. P. Gary, and J. Wang, *J. Geophys. Res.* **101**, 10749 (1996).
14. S. P. Gary, R. M. Skoug, and W. Daughton, *Phys.of Plasmas* **6**, 2607 (1999).
15. S. P. Gary, S. Saito, and H. Li, *Geophys. Res. Lett.* **35** (2008).
16. S. Saito, and S. P. Gary, *J. Geophys. Res.* **112** (2007).
17. A. D. Johnstone, and et.al., *Space Sci. Rev.* **79**, 351 (1997).
18. A. F. Viñas, and C. Gurgiolo, *J. Geophys. Res.* **114** (2009).
19. G. Gustafsson, and et. al., *Space Sci. Rev.* **79**, 137 (1997).
20. A. Balogh, and et. al., *Space Sci. Rev.* **79**, 65 (1997).
21. H. Réme, and et. al., *Space Sci. Rev.* **79**, 303 (1997).
22. S. P. Gary, *Theory of Space Plasma Microinstabilities*, Cambridge Univ. Press, New York, NY, USA, 1993.
23. F. Sahraoui, M. L. Goldstein, P. Robert, and Y. V. Khotyaintsev, *Phys. Rev. Lett.* **102**, 231102 (2009).